54th AIAA Aerospace Sciences Meeting, January 4 - 8 2016, San Diego, CA

Effects of Upstream Disturbances on a Pitching NACA0012 Airfoil

Brandon E Merrill* and Yulia Peet†

Dynamically moving airfoils are encountered in several areas of flight and energy production, including helicopter rotors, wind turbine blades, and maneuvering aircraft. A clearer understanding of how freestream disturbances affect the aerodynamic forces on pitching airfoils leads to improvements in aircraft and wind turbine design. In the present study, our recently validated moving overlapping mesh methodology is used to perform a direct numerical simulation of a NACA0012 airfoil pitching with oscillatory motion in the presence of a turbulent wake created by an upstream cylinder. The global computational domain is decomposed into a stationary background mesh, which contains the cylinder, and a mesh constructed around the airfoil that is constrained to pitch with predetermined reduced frequency, k=0.16. Present simulations are performed with chord based Reynolds number Re$_c = 44,000$, with aerodynamic forces and vortex shedding properties being compared between the pitching airfoil simulations with and without upstream disturbances.

I. Introduction

A greater understanding of the aerodynamic forces acting on airfoils with a wide variety of flow conditions is imperative in creating flexible models to improve the fidelity of large scale aerodynamic simulations. While many aspects of airfoil aerodynamics have been examined in depth, several facets have traditionally been difficult to measure or simulate. The flow around pitching airfoils is one facet of research that has been studied for several decades, although much is unknown regarding the nature of the flow when unsteady flow conditions are present. The flow around pitching airfoils, especially as it relates to dynamic stall, has ramifications for the efficiency and design of helicopter rotors,[1,2] wind turbines,[3] other rotating machinery such as compressors,[4] as well as extensions to the maneuverability of fixed wing aircraft.[5,6]

The general characteristics of pitching airfoils and mechanisms of dynamic stall are well understood in the presence of steady inflow conditions, and several experimental and computational projects have examined this topic. The lift force on a dynamically pitching-upward airfoil with steady inflow will generally increase up to an angle of attack beyond its static stall angle until dynamic stall occurs. As an airfoil pitches upward, a large vortex, referred to as a dynamic stall vortex (DSV), forms at the leading edge of an upward pitching airfoil, creating a low pressure region, which then travels along the suction side of the airfoil toward the trailing edge. The lower pressure on the suction side of the airfoil increases the lift, until the vortex nears the trailing edge where it separates and a dramatic decrease in lift, dynamic stall, ensues. Dynamic stall research typically focuses on the effects of altering pitching frequency, pitching amplitude, Reynolds number, and Mach number, as well as possible ways to gain greater control of dynamic stall.[7–12] However, unsteady inflow conditions can also play a crucial role in the aerodynamics of pitching and plunging airfoils. Blades on wind turbines operating in yawed or unsteady flow conditions, for instance, experience inflow velocity that is periodic with respect to azimuthal angle.[13,14] Turbulence, gusts, and vortices caused by upstream structures, objects, or atmospheric conditions create unsteady inflow for helicopter rotors, wind turbine blades, and wings on maneuvering aircraft. In order to create a more complete realization of dynamic stall phenomena, the various velocity fluctuations commonly experienced by pitching airfoils in realistic situations need to be included in future research and simulations.

At the present time, some experimental research has been performed to examine the effects of unsteady inflow on pitching airfoils, while a much smaller amount of computational work has been done in this area. In

---

*PhD Candidate, School for Engineering of Matter, Transport, and Energy (SEMTE), Arizona State University; Email: brandon.merrill@asu.edu

†Assistant Professor, School for Engineering of Matter, Transport, and Energy (SEMTE), Arizona State University

the 1970's Pierce et al.[2] and Kottapalli et al.[15] performed experiments on pitching helicopter blades using a gust generator to produce periodic inflow conditions. Their results show that the varying freestream velocity affects the pitching moment and drag experienced by the blade, and that the magnitudes of the forces and moment change depending on the phase difference between the airfoil oscillation and inflow velocity oscillation. Similar experimental investigations have been performed more recently by Shi and Ming on a pitching delta wing, for improvements in the design of super-maneuverable aircraft.[5,6]

Experimental investigations of turbulence effects on pitching airfoils have been performed by Conger et al.,[16] Laneville et al.,[17] and Chen et al.[18] In the study by Chen et al., a turbulent wake was generated upstream of a ramping airfoil by placing a small cylinder in the flow field. The experiment had a relatively low chord based Reynolds number of 80,000. The effects of varied cylinder position with respect to the airfoil was studied to compare the aerodynamic forces and moments with those experienced by a pitching airfoil in steady freestream. Their work showed that dynamic stall events occur at larger angles of attack in the presence of a turbulent wake when compared to steady inflow cases, although different vertical positions of the cylinder had differing effects on the aerodynamic forces.

Little computational research has been performed regarding pitching airfoils with unsteady freestream flow due to the difficulty of traditional computational fluid dynamics (CFD) solvers in handling moving geometries with non-uniform inflow conditions, as well as the computational cost of such simulations. Recent research published by Gharali et al.[13,19] investigates two-dimensional pitching airfoils in the presence of periodic inflow velocity using an Unsteady Reynolds Averaged Navier-Stokes (URANS) solver. However, no known computational simulations of pitching airfoils have been performed with turbulent inflow conditions, yet information from such simulations would be pivotal in improving the fidelity of large scale models of systems with realistic flow conditions. These enhanced models lead to improvements in the physical design of aircraft and wind turbines.

Our newly developed and validated moving overlapping mesh methodology allows us to decompose the global computational domain into a moving mesh and a stationary mesh. By enabling an entire mesh to move, consistent resolution near the solid boundary of a moving object is easily maintained. A stationary background mesh allows for unsteady boundary conditions to be straightforwardly implemented in the lab reference frame, and for stationary objects to be placed elsewhere in the flow field. The formulation is currently built within a spectral element method (SEM) incompressible flow solver (Nek5000[20]), and maintains the global spectral spatial accuracy of the underlying solver.[21]

The present project simulates a NACA0012 airfoil with oscillatory pitching motion and chord based Reynolds number $Re_c = 44,000$. We investigate its interactions with a turbulent wake generated by a small stationary cylinder, with diameter based Reynolds number $Re_D = 3900$, that disturbs the upstream flow. A mesh is created around the three-dimensional extruded airfoil and motion is prescribed to the entire mesh. This moving airfoil mesh is placed within a stationary background mesh that contains the cylinder. Aerodynamic coefficients and the pressure values at the airfoil surface are compared between simulations with and without the upstream disturbance. We present results that give a clearer understanding of the largely unknown effects of disturbances on dynamic stall and oscillating airfoils in general. Results from initial simulations performed without upstream disturbances are compared with experimental results of Panda and Zaman[22] who approximate the lift force on an oscillating airfoil using vorticity measurements in the near wake.

II. Methods

Our moving overlapping mesh methodology is employed within the Nek5000 computational fluid dynamics framework[20] which utilizes the Spectral Element Method (SEM) for spatial discretization, and allows for up to third order temporal discretization for solutions to the incompressible Navier-Stokes equations (1).

$$\begin{gathered}\frac{\partial \mathbf{u}}{\partial t} + \mathbf{u}\cdot\nabla\mathbf{u} = -\nabla\mathbf{p} + \frac{\mathbf{1}}{\mathrm{Re}}\nabla^{\mathbf{2}}\mathbf{u} \\ \nabla\cdot\mathbf{u} = \mathbf{0}\end{gathered} \tag{1}$$

Spatial discretization is performed by dividing each subdomain into a set of elements wherein the solution is approximated using polynomial basis functions that pass through a discrete number of collocation points with Gauss-Lobatto Legendre (GL) point distribution for velocity and Gauss Legendre (G) point distribution for pressure. Exponential spatial convergence is achieved with polynomial order refinement, which thus increases the number of GL and G points defined within each element. The moving overlapping mesh methodology has previously been shown to maintain this exponential spatial accuracy in the global computational domain.[21] Stability is achieved with minimal Schwarz-like iterations[23] (usually two or three) while maintaining temporal accuracy that is consistent with the global time integration scheme.[21] The method allows for large ranges of mesh motion and flexibility of the mesh to translate or rotate in two- and three-dimensional simulations. Parallel computations achieve linear scaling to thousands of processors.

Within the formulation, a global domain, Ω, is decomposed into two overlapping subdomains, Ω^1 and Ω^2. Velocity values are exchanged at subdomain interfaces, Γ^{12} and Γ^{21}, and the mesh defined in subdomain Ω^i is prescribed a predetermined rotational or translational velocity $\mathbf{w}^{[i]}$ (see Figure 1). Dirichlet conditions are enforced on moving wall boundaries, $\partial\Omega_w$, that match the velocity of the moving rigid body.

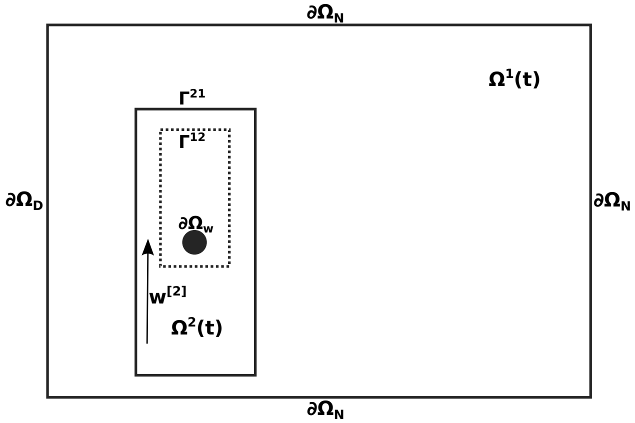

Figure 1. Illustration of a decomposed global domain. Dashed lines denote a hole cut in the background mesh.

II.A. Handling Interfaces Between Meshes

Values at mesh interfaces, Γ^{ij}, are determined by performing Lagrangian interpolation on values in the adjacent subdomain from previous timesteps. This interpolation method, when coupled with the SEM solver, gives spectrally accurate values at gridpoints on interface boundaries. *Search and locate* procedures are carried out to express the location of a point on the interface of one subdomain (Ω^i) in terms of the local coordinates of a corresponding element in the other subdomain (Ω^j). The problem is treated as an optimization task, seeking to minimize residuals with the Newton-Raphson method.[24] Temporal coupling at interfaces is performed using an mth-order explicit interface extrapolation (IEXTm) scheme, using interpolated values from previous timesteps. The m^{th} order extrapolation operator is given in equation 2 with the coefficients γ_{pm} given in table 1.

$$E_m\left[u\right]^n = \sum_{p=1}^{m} \gamma_{pm} u^{n-p} \tag{2}$$

Table 1. Coefficients for the EXTm schemes, m=1,2,3[25]

	γ_{p1}	γ_{p2}	γ_{p3}
p=1	1	2	3
p=2		-1	-3
p=3			1

Stability of the extrapolation method has been examined using the one-dimensional unsteady diffusion equation on two stationary overlapping subdomains with uniform point distribution. The grids overlapped to ensure the grid points in the two domains coincided. The stability for the extrapolation scheme in the study was confirmed analytically to be unconditionally stable for first order extrapolation with the backwards-differentiation scheme of first or second order. For higher orders, the stability is dependent upon the mesh overlap size and the number of extrapolation iterations.[25] While a stability analysis of the extrapolation scheme used with moving grids is not available, practice has shown that global stability is achieved for moving subdomain simulations with two or three iterations.

II.B. Arbitrary Lagrangian-Eulerian Formulation

Subdomain movement is handled with the Arbitrary Lagrangian-Eulerian (ALE) formulation, which combines the attractive properties of both the Lagrangian formulation, where the reference system is attached to 'particles' in the fluid, and Eulerian formulation, where the reference system is fixed in space. One of its primary advantages is the ability to assign an arbitrary velocity to discrete points on the mesh. The velocity assigned to the mesh can be determined by some property of the flow, or it can be predetermined and its movement unaffected by the flow. The explanation and derivation of the ALE formulation below follows the general process given by Deville et al.[26]

The material derivative of a variable, f, given by

$$\frac{Df}{Dt} = \frac{\partial f}{\partial t} + \mathbf{u} \cdot \nabla f \tag{3}$$

where $\mathbf{u}(\mathbf{x}, t)$ is the velocity of the fluid in the Eulerian formulation, describes the time evolution of f attached to material points. If velocity $\mathbf{w}(\mathbf{x}, t)$ is assigned to the computational domain, and $\mathbf{w}(\mathbf{x}, t) \neq \mathbf{u}(\mathbf{x}, t)$, a pseudo-material derivative can be defined for the moving domain, as if virtual particles are moving in accordance with the domain, which we will call the ALE derivative

$$\frac{\delta f}{\delta t} = \frac{\partial f}{\partial t} + \mathbf{w} \cdot \nabla f \tag{4}$$

Note that if $\mathbf{w}(\mathbf{x}, t) = 0$ we recover the Eulerian description, or simply the partial time derivative, and if $\mathbf{w}(\mathbf{x}, t) = \mathbf{u}(\mathbf{x}, t)$ we arrive at the material derivative in the Lagrangian description. A relative velocity, $\mathbf{c}$, is defined with respect to the reference frame of the moving mesh

$$\mathbf{u} = \mathbf{c} + \mathbf{w}, \tag{5}$$

and the relationship between the material and ALE time derivative can then be given as

$$\frac{Df}{Dt} = \frac{\delta f}{\delta t} + \mathbf{c} \cdot \nabla f. \tag{6}$$

To account for mesh movement, the convective terms in the Navier-Stokes equations are altered to reflect the new relative velocity, $\mathbf{c}$.[27] Since density is held constant for incompressible flow, the convective term of the mass conservation equation is zero, and therefore, there is no change in the continuity equation. The momentum conservation equation becomes

$$\frac{\delta \mathbf{u}}{\delta t} + \mathbf{c} \cdot \nabla \mathbf{u} = -\nabla \mathbf{p} + \frac{\mathbf{1}}{\mathrm{Re}} \nabla^{\mathbf{2}} \mathbf{u}. \tag{7}$$

Again, note that if mesh velocity $\mathbf{w}$ is equal to zero, the original Navier-Stokes equations (equation 1) are recovered. Upon discretization, each gridpoint is assigned its own velocity value, allowing for flexible movement, including rotation, although care must be taken to not excessively deform the grid.

II.C. Communicating Updates

In the present methodology, physical coordinates of gridpoints that lie on a moving subdomain's interface boundaries change with each timestep. The physical coordinates of gridpoints in the stationary subdomain remain constant, although the relative positions of its interface points with respect to the adjacent subdomain constantly change due to movement of the adjacent subdomain. Thus, updated coordinates are determined and communicated once per timestep for each subdomain. Upon communication, the search and locate procedures are performed to determine precise locations of interface points within the other subdomain, and spectral interpolation is carried out to determine accurate velocity values. Once velocity values are assigned to points on the interfaces, those boundaries are treated as Dirichlet conditions, and each subdomain completes its computations for the current timestep without any additional communications to or from the other subdomain.

III. Results

To determine the effect of turbulent wakes on pitching airfoils a three-dimensional global computational domain is decomposed into two overlapping subdomains. A mesh constructed around a NACA0012 airfoil is constrained to move with a predetermined pitching motion, and a stationary background mesh contains a small cylinder to generate the turbulent wake (a background mesh without a cylinder is also used for baseline results, see Figure 2). All simulations are performed with chord-based Reynolds number of, $\mathrm{Re}_c = 44,000$. Pitching airfoil simulations are performed using 6^{th}-order polynomial approximations for spatial discretization within each element, and dynamic timestepping with a maximum timestep of $\Delta t^*_{max} = 2 \times 10^{-4}$, although the average timestep in the simulations is approximately $\Delta t^*_{avg} \approx 5 \times 10^{-5}$, where time is nondimensionalized with the freestream velocity and chord length, $t^* = tU_\infty/c$. Dynamic timestepping is used to ensure that sufficient temporal resolution is achieved while allowing efficient use of computational resources. Simulations use second order time integration with IEXT2 at interface boundaries. Two cases will be compared as presented in Table 2

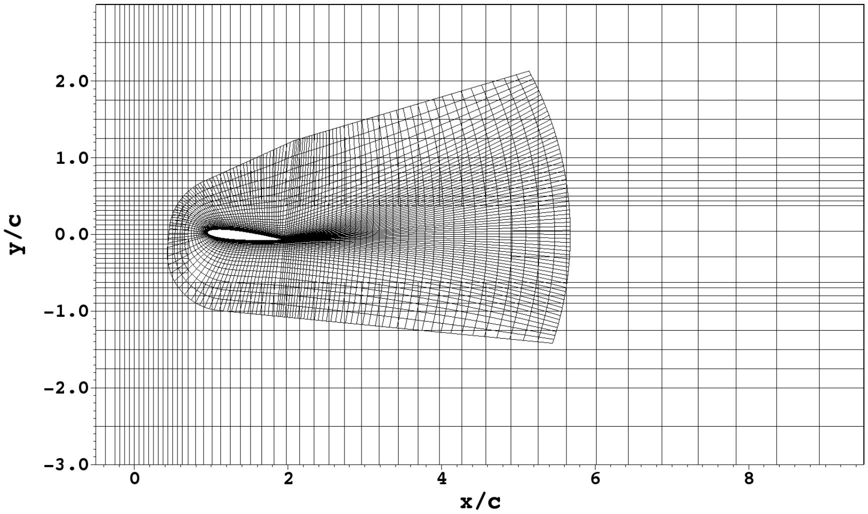

Figure 2. A cross section of the global computational domain for steady inflow simulations, showing element boundaries of the moving airfoil mesh within the stationary background mesh.

Case	Position of Cylinder $(\frac{x}{c}, \frac{y}{c})$	Position of Airfoil Quarter-Chord $(\frac{x}{c}, \frac{y}{c})$
I	No Cylinder	(1.2, 0)
II	(0, 0)	(1.2, 0)

Table 2. Pitching airfoil cases.

The aerodynamic coefficients of lift, drag, and pitching moment acting on the airfoil are calculated as

$$C_L = \frac{L}{\frac{1}{2}\rho U_\infty^2 S} \tag{8}$$

$$C_D = \frac{D}{\frac{1}{2}\rho U_\infty^2 S} \tag{9}$$

$$C_M = \frac{M}{\frac{1}{2}\rho U_\infty^2 S c}, \tag{10}$$

where L is the lift force, D is the drag force, M is the pitching moment (or torque), ρ is fluid density, U_∞ is the inflow velocity, S is the planform area, and c is the chord length.

III.A. Oscillating Airfoil at $Re = 44,000$

Here we discuss the results of Case I, which are used as a baseline for comparison with Case II. The meshes for the the present case, as displayed in Figure 2, are prescribed steady inflow conditions on the left side

($u = U_\infty$), outflow conditions on the right side, and symmetry conditions on the top and bottom of the global domain. The domain has a spanwise width of z/c=0.2, with periodic conditions prescribed on the spanwise boundaries. Moving wall boundary conditions are prescribed at the surface of the airfoil, outflow conditions are prescribed at the right boundary of the airfoil mesh, while all other interior boundaries in the airfoil and background meshes use interface conditions to pass values between subdomains. The airfoil mesh contains 54k elements (19M gridpoints) and the background mesh contains 16k (5M gridpoints). Grid spacings at the airfoil surface are given in Table 3.

$\Delta s_U/c$	$\Delta s_L/c$	$\Delta n/c$	$\Delta z_{min}/c$	$\Delta z_{max}/c$
6.4×10^{-3}	9.0×10^{-3}	4.5×10^{-5}	1.3×10^{-3}	4.2×10^{-3}

Table 3. Airfoil grid parameters for present pitching airfoil simulations: maximum streamwise GL point spacing on the upper ($\Delta s_U/c$) and lower ($\Delta s_U/c$) surfaces of the airfoil, normal spacing on the upper airfoil surface at the mid-chord location ($\Delta n/c$), and the minimum ($\Delta z_{min}/c$) and maximum ($\Delta z_{max}/c$) spanwise GL point spacing.

The angle of attack for the NACA0012 airfoil pitching about its quarter-chord axis is prescribed as

$$\alpha = 15.3^\circ - 9.7^\circ \cos\left(2\pi f t\right), \tag{11}$$

where the reduced frequency is $k \equiv \pi f c/U_\infty = 0.16$.

Simulation results are compared with the experimental results of Panda and Zaman,[22] who used probes in the wake of an oscillating airfoil collect velocity and vorticity data of the flow in the wake. The unsteady lift force, reported in Ref. 22, is divided into a *non-circulatory* component and a *circulatory* component according to Bisplinghoff et al.,[28] where Panda and Zaman used the experimental wake data to approximate only the circulatory component of the lift force acting on the airfoil. While the addition of the non-circulatory component would change the value of the total lift force, the difference is fairly minor, and even negligible at small reduced frequencies, and thus the total lift coefficient values from the present simulation is compared with only the circulatory component of lift that is published in Ref. 22.

Three methods are described in Panda and Zaman[22] for approximating the circulatory component of lift by integration of the phase averaged measured vorticity data. The authors state that an unknown steady contribution to the lift approximation exists due to vortices shed before the start of data collection, and thus the lift is assumed to be zero at the minimum angle of attack in their lift coefficient plots. In the plots below, data from Ref. 22 is shifted to give a lift value that matches present simulations at the minimum angle of attack.

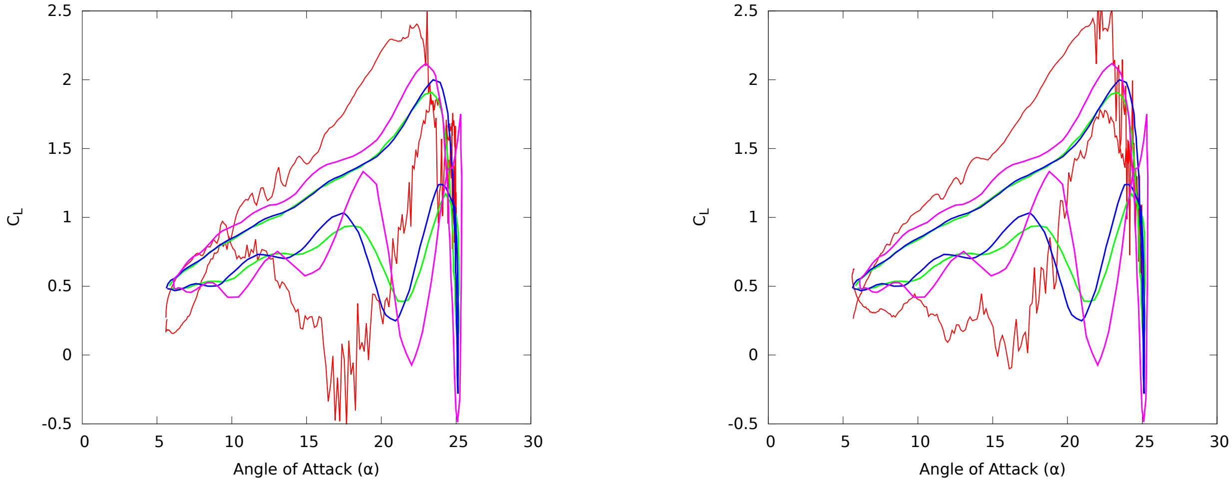

(a) 1^{st} Cycle (b) 2^{nd} Cycle

Figure 3. Lift coefficients from present tests compared with approximations derived from experimental wake surveys by Panda and Zaman.[22] The red curves represent present simulation data for Case I, while the green, blue, and magenta lines represent the circulatory component of the lift coefficient approximated from experimental wake data, which was phase averaged over 80 cycles, using methods 1, 2, and 3, respectively as published in Panda and Zaman.[22]

Figure 3 presents the lift coefficient values for present simulations compared with the experimental approximations.[22] Performing phase averages for simulations over 80 cycles, as was done for the experimental data, is not feasible considering the computational resources it would require, thus the instantaneous simulation data is compared with the phase averaged experimental approximations. We see that while the general shapes of the curves are the same, the present simulation data reports higher lift values than the experimental approximation, and though lift values during downstroke do not exactly follow the experimental approximations, the same features are present, namely a local minimum near $\alpha = 25°$ followed by an increase in lift, then another stall event. Following the major stall event during the downstroke, the lift values oscillate, in both simulation and experimental data, until the airfoil reaches its minimum angle of attack, $\alpha = 5.6°$, after which it begins the next cycle. It is expected that averaging simulation data over many cycles would produce better correlation with the experimental results.

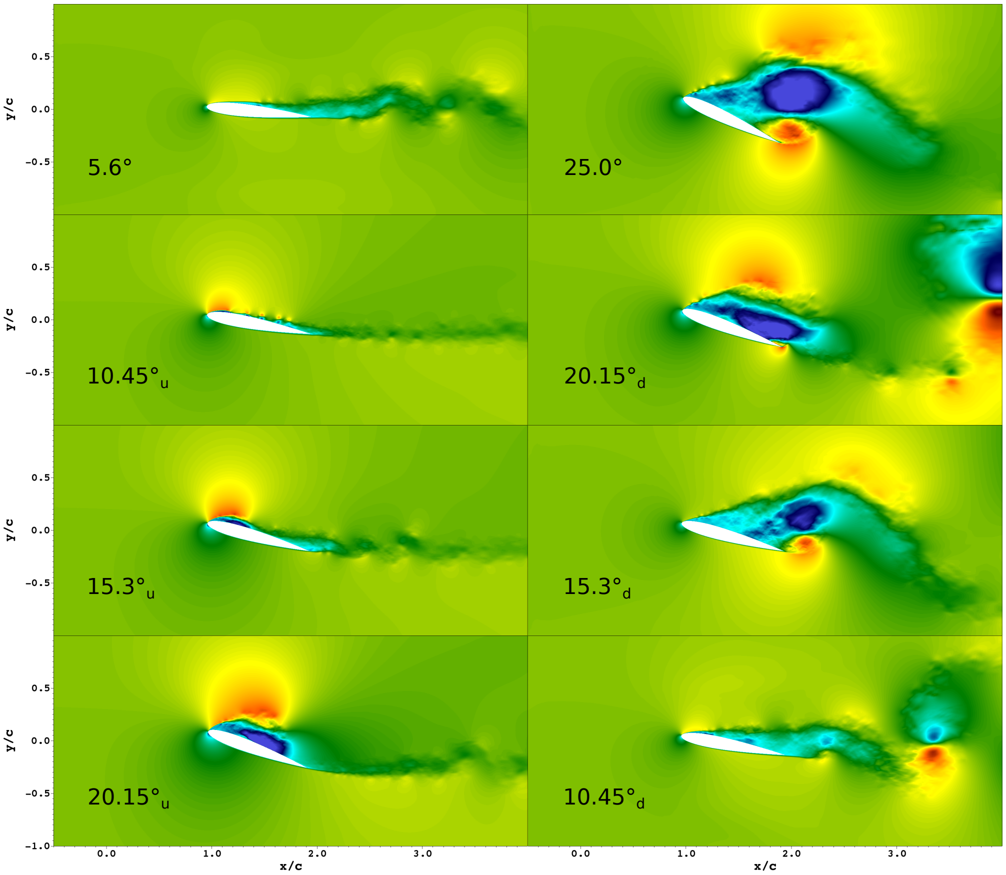

Figure 4. Zoomed-in spanwise averaged streamwise velocity plots during the second cycle, at angles of attack posted in bottom left corner of each snapshot. The subscript 'u' denotes upstroke and 'd' downstroke. Darkest blue represents streamwise velocity less than $u/U_\infty = -1$, and darkest red greater than $u/U_\infty = 3$

Visualizations of the the spanwise averaged streamwise velocity (Figure 4) and spanwise vorticity (Figure 5) show the clockwise rotating dynamic stall vortex (DSV) forming and traveling toward the trailing edge as the airfoil pitches upward. As the DSV nears the trailing edge, a counter-clockwise trailing edge vortex (TEV) forms, which first appears in the $\alpha = 25°$ frames. When the airfoil begins its downstroke, another clockwise vortex forms at the leading edge, which is smaller than the original DSV, and travels along the upper surface of the airfoil until it detaches, causing another stall event.

By comparing the pressure coefficient values along the upper surface of the airfoil (Figure 6) with the streamwise velocity (Figure 4) and spanwise vorticity (Figure 5) plots we see that the position of low pressure valleys correlate with the location of vortex centers. Evidence of the forming DSV is found in the $\alpha = 10.45^\circ_u$ curve by the low pressure at the leading edge of the airfoil. We see that the low pressure region propagates toward the trailing edge of the airfoil in the $\alpha = 15.3^\circ_u$ and $\alpha = 20.15^\circ_u$ curves. When the airfoil reaches its maximum angle of attack the DSV has already detached, though in the $\alpha = 25.0°$ curve we find evidence of the TEV at the trailing edge of the airfoil. The $\alpha = 20.15^\circ_d$ curve shows that the pressure values corresponding to the second major vortex are not as low as the initial DSV, though we see that the resulting TEV creates a sharp pressure valley at the trailing edge.

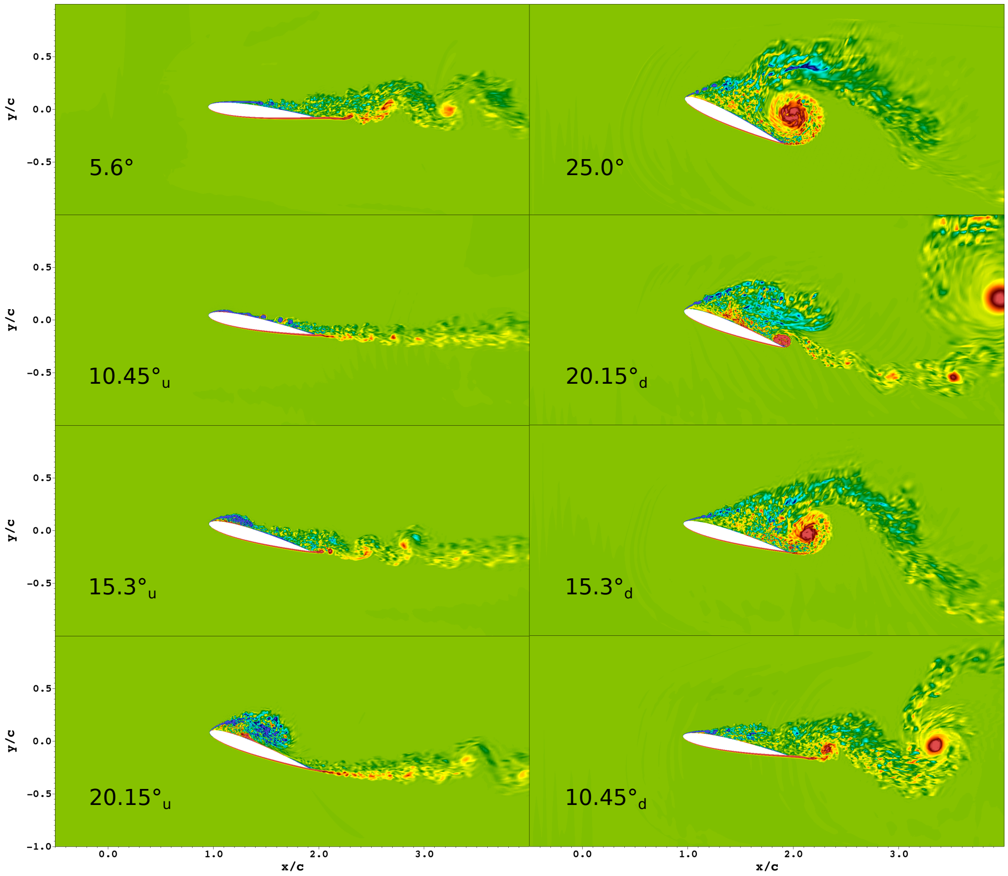

Figure 5. Zoomed-in spanwise averaged spanwise vorticity plots during the second cycle, at angles of attack posted in bottom left corner of each plot. The subscript 'u' denotes upstroke and 'd' downstroke. Darkest blue represents spanwise vorticity of less than $\omega_z U_\infty / c = -40$ (corresponding with clockwise fluid motion), and darkest red greater than $\omega_z U_\infty / c = 40$ (corresponding with counter-clockwise fluid motion).

An indication of the strength of the DSV is obtained by performing a volume average of the spanwise vorticity over a cylindrical volume centered at the vortex center:

$$\Gamma \equiv \frac{\left| \int_{V_{cyl}} \omega_z^* \, \mathrm{d}V_{cyl} \right|}{V_{cyl}}, \tag{12}$$

where V_{cyl} is the volume of the cylinder being considered, and the non-dimensional spanwise vorticity, $\omega_z^* \equiv \omega_z U_\infty / c$. The center of the vortex is located by finding the local spanwise vorticity minimum in the spanwise averaged vorticity field. The strength of the DSV (Γ) is determined as the center reaches the $x/c = 1.95$ position in the flow field, and integration is performed over a cylindrical volume with radius of $r/c = 0.25$, as illustrated in Figure 7, and width, $z/c = 0.2$, which corresponds to the span of the domain. Table 4 presents properties of the DSV at during this snapshot.

Vortex Center ($\frac{x}{c}, \frac{y}{c}$)	(1.95,0.127)
Time (t^*)	27.9
Angle of Attack (α)	23.83^o_u
Vortex Strength (Γ)	10.547

Table 4. Properties of the DSV during the second pitching cycle of Case I as the center of the vortex reaches the $x/c = 1.95$ position in the flow field.

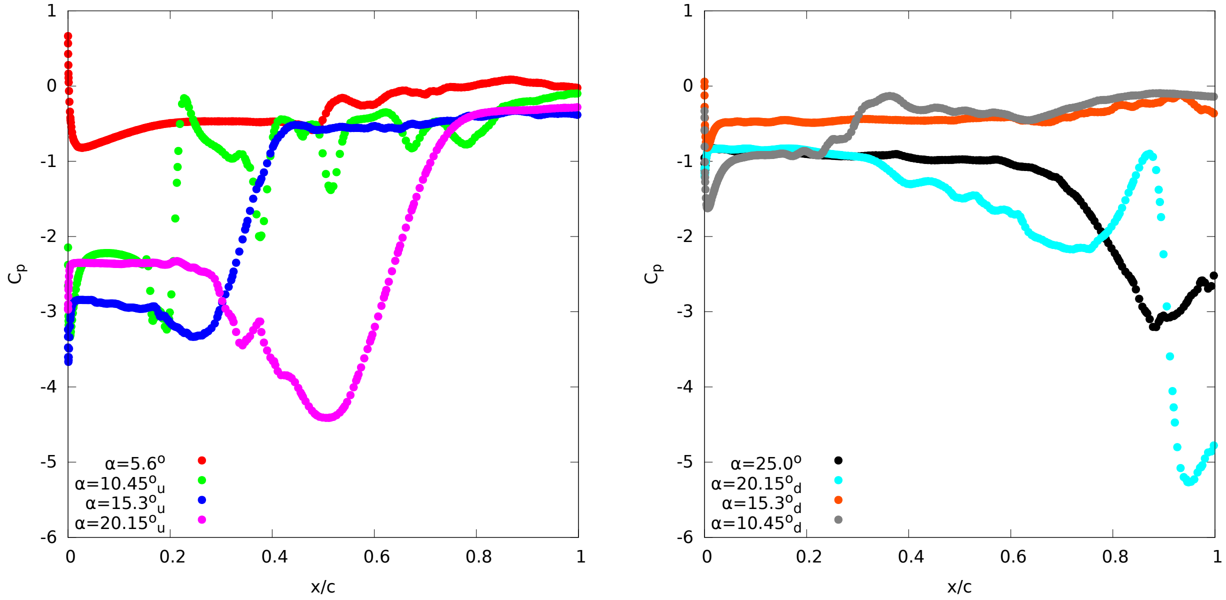

(a)

(b)

Figure 6. Pressure coefficient values along the suction surface of the airfoil at posted angles of attack. The pressure coefficient values are averaged in the spanwise direction. The subscript 'u' denotes upstroke and 'd' downstroke.

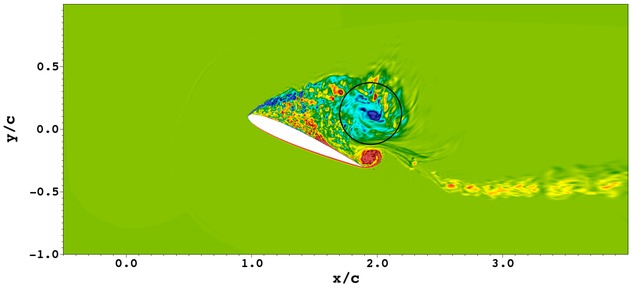

Figure 7. Spanwise averaged spanwise vorticity plot when the center of the DSV during the second cycle reaches $x/c = 1.95$ ($t^* = 27.9$, $\alpha = 23.83^o_u$) **for Case I. The circle outlines the volume over which the integral of vorticity is taken.**

III.B. Pitching Airfoil in a Turbulent Wake

In this section we discuss Case II, which is performed using the airfoil mesh presented in Section III.A, but with a background mesh that contains an upstream cylinder for the generation of a turbulent wake, as illustrated in Figure 8. For a description of boundary conditions refer to Section III.A, with the addition of stationary wall boundary conditions enforced on the upstream cylinder.

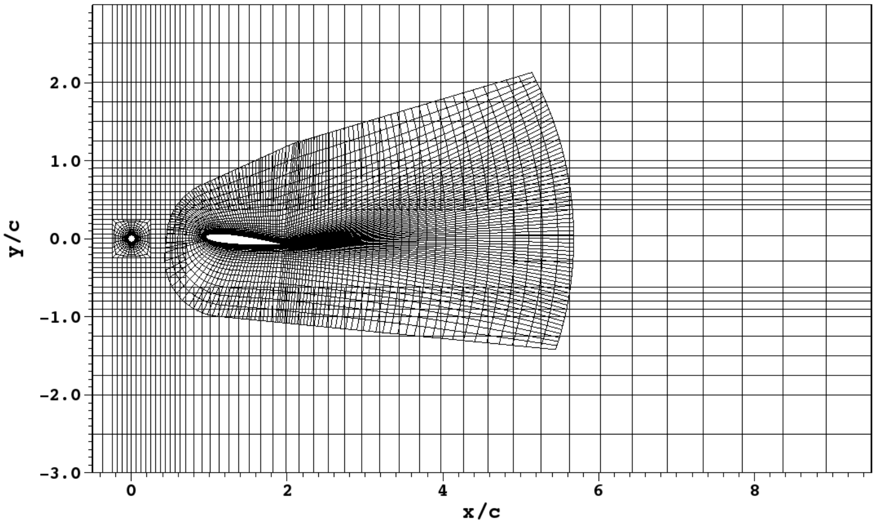

Figure 8. Mesh configuration for simulations of an oscillating airfoil in the presence of a turbulent wake. Only element boundaries are shown.

In the global computational domain, the horizontal distance from the center of the cylinder to the pitching axis (quarter-chord) of the airfoil is $x = 1.2c\,(\approx 13.5D)$, in terms of chord lengths (and cylinder diameters). To give a diameter based Reynolds number of 3900 in a flow with chord based Reynolds number of 44,000, the diameter of the cylinder relative to the chord length of the NACA0012 airfoil is $D/c \approx 8.86 \times 10^{-2}$. All future length units will be nondimensionalized with respect to the chord length of the airfoil. The spanwise width of the global domain is $z/c = 0.2$. The airfoil begins its first cycle at time zero, before the cylinder wake has developed. Thus, the ensuing discussion will focus on the second cycle of the airfoil motion (although the first cycle is also shown for completeness), where the turbulent wake is fully developed for the entire region where the airfoil resides when the second cycle begins.

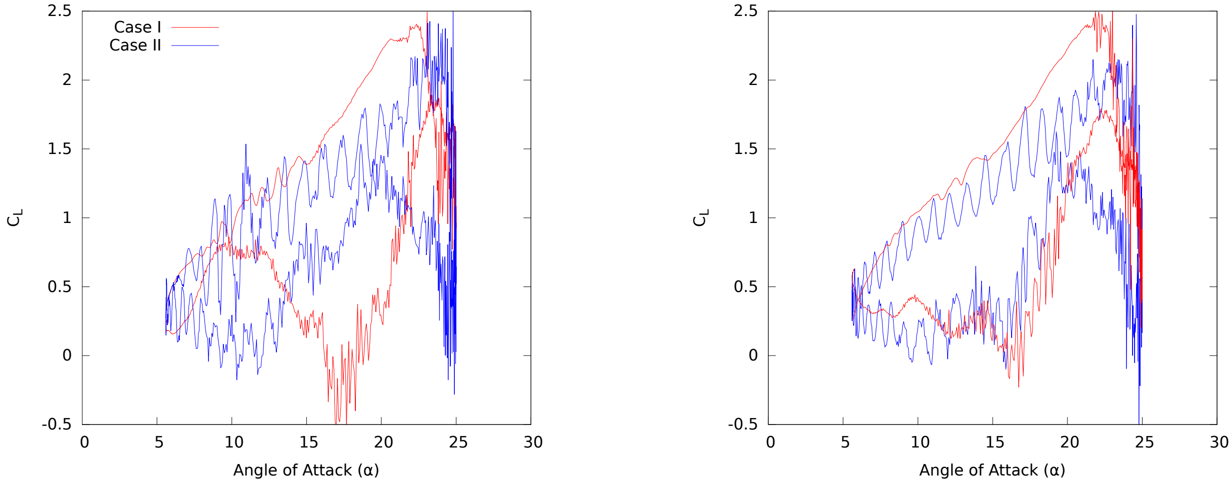

(a) 1^{st} Cycle

(b) 2^{nd} Cycle

Figure 9. Lift coefficient results from Case II compared results from Case I for the first and second cycles.

A comparison of the lift coefficient loops between Cases I and II (Figure 9) shows stark differences in the lift that the airfoils experience in each case. The lift acting on the airfoil in Case II is quite oscillatory due to the incoming turbulent vortices shed from the upstream cylinder. We see that in Case I, the lift increases at a slightly steeper rate starting at $\alpha \approx 15^o_u$, which corresponds to the formation of the DSV and its path along the upper surface of the airfoil. In Case II we do not find evidence of a steeper rate of lift increase, and in the second cycle we see that the maximum lift caused by the DSV does not reach as great a value as seen in Case I. While some of the sharp lift oscillations in Case II temporarily give lift values of the same, or even greater, magnitude when compared with Case I, the general trend shows lift values that are lower for the disturbed case in both lift peaks. In the second cycle, the minimum lift values in both cases are comparable.

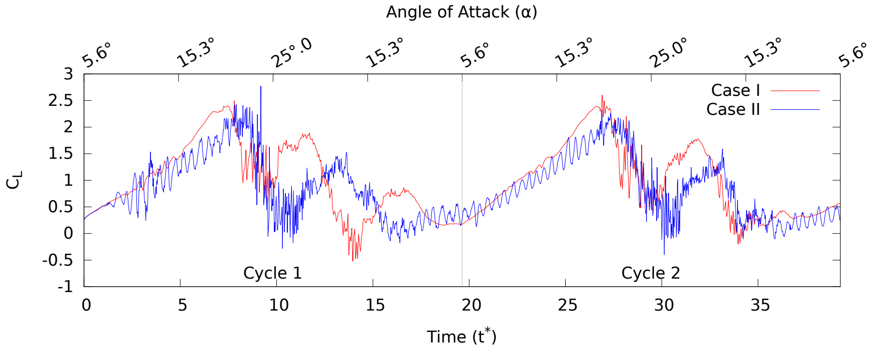

(a) Lift Coefficient

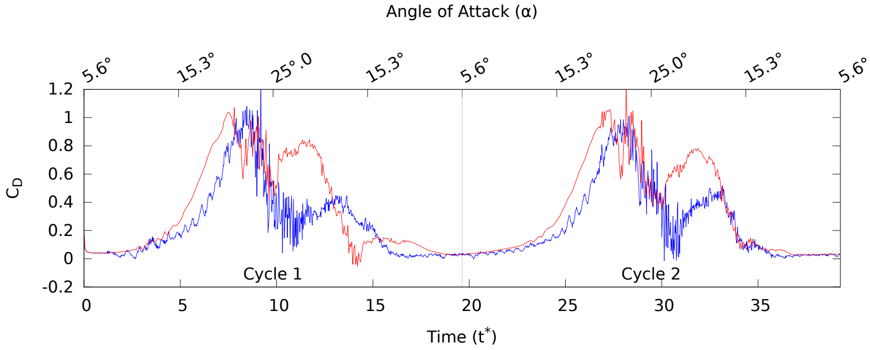

(b) Drag Coefficient

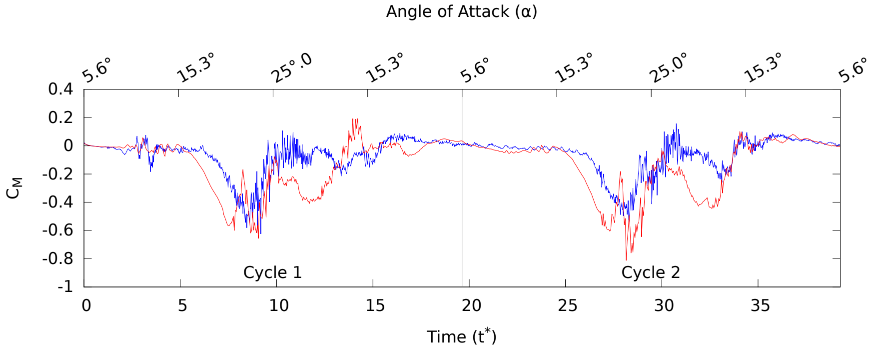

(c) Pitching Moment Coefficient

Figure 10. Aerodynamic forces and moments from Case II compared with results from Case I for the first and second cycles. The time ($t^* = tU_\infty/c$) is labeled along the bottom axis while the corresponding angle of attack is along the top axis.

Figure 10 displays the aerodynamic forces and moments acting on the airfoil in Cases I and II with respect to time. In cycle two, Case I reports a global maximum lift of $C_L \approx 2.67$ at $\alpha \approx 23.7^o_u$, while Case II reports a global maximum lift of $C_L \approx 2.48$ at $\alpha \approx 24.6^o_u$. A second lift peak, due to a second major vortex formed during airfoil downstroke, occurs at $\alpha \approx 22.2^o_d$ in Case I reporting a lift value $C_L \approx 1.79$, while the second lift peak of Case II is reported at a much later time with $\alpha \approx 19.3^o_d$ and local maximum lift $C_L \approx 1.62$. We see that stall occurs at a later time in Case II for both the DSV and second major vortex, similar to the results of Chen and Choa[18] which showed that stall of a constant rate pitching airfoil occurs at a later time when upstream disturbances are present.

Evidence of stall is seen in the drag values as well, with a steep decrease in drag when stall occurs. After initial stall occurs in Case I, a steep increase in drag immediately ensues reaching drag values comparable to the first peak. This second drag peak correlates with the formation of the TEV, and a sharp decrease in drag is again witnessed as the TEV detaches. Case II does not show clear signs of this large drag peak due to the TEV. While the drag acting on the airfoil in Case II almost reaches the same global maximum values of Cases I (though at a later time), the drag in nearly all other portions of the cycle is greatly reduced by upstream disturbances. We see particular evidence of this when looking at the drag peak due to the second major vortex formed during the airfoil downstroke, where Case II reports a local drag maximum of $C_D \approx 0.52$ at $\alpha \approx 19.3^o_d$, where the drag reported in Case I is about 50% larger with $C_D \approx 0.79$ at $\alpha \approx 22.2^o_d$.

The *magnitude* of the pitching moment of the airfoil remains small until a large vortex begins to form on the leading edge of the airfoil, when a sharp increase in the *magnitude* of the pitching moment is seen (to large negative values) and continues to increase until the vortex detaches from the surface of the airfoil. In Case I, large fluctuations in the pitching moments are seen for the majority of the cycle, while in Case II, we see a large fluctuation in the pitching moment as a result of the DSV (though not as large as in Case I), but the pitching moment remains near zero for the remainder of the cycle. Thus we see that the turbulent wake incident upon the pitching airfoil alleviates much of the strong pitching moments the airfoil experiences.

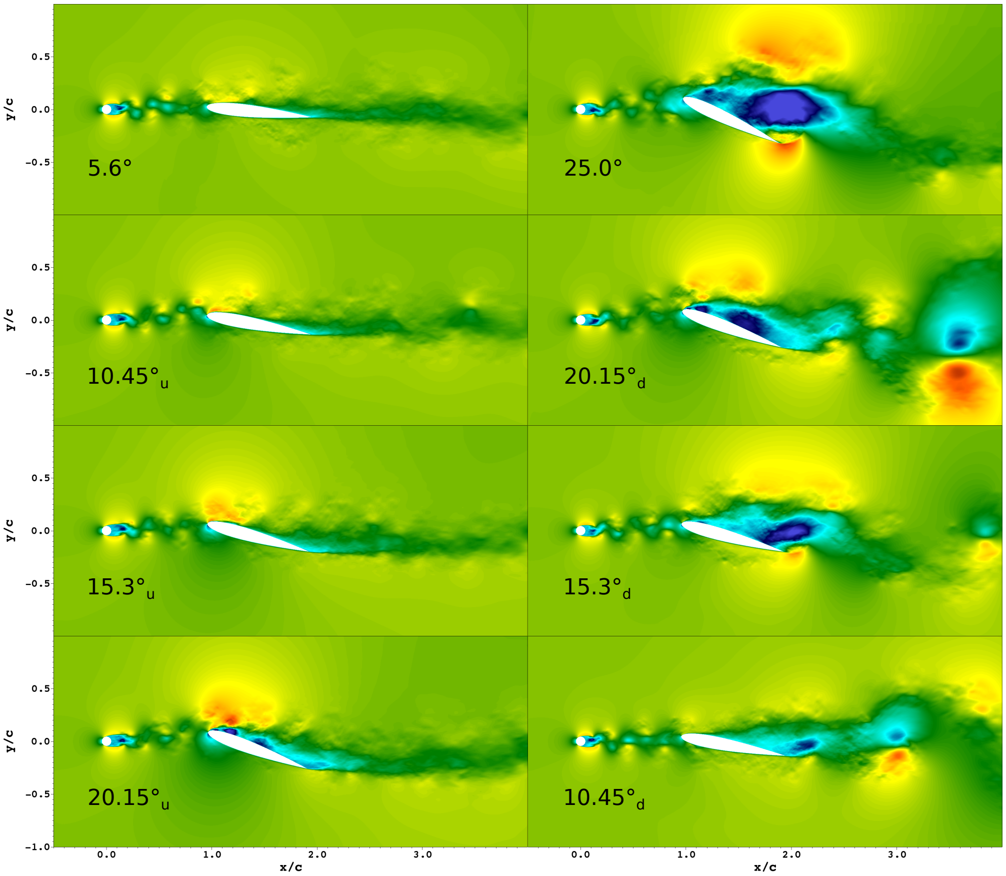

Figure 11. Zoomed-in spanwise averaged streamwise velocity plots of Case II during the second cycle, at angles of attack posted in bottom left corner of each snapshot. The subscript 'u' denotes upstroke and 'd' downstroke. Darkest blue represents streamwise velocity less than $u/U_\infty = -1$, and darkest red greater than $u/U_\infty = 3$

Visual inspection of the spanwise averaged streamwise velocity (Figure 11) and spanwise vorticity (Figure 12) for Case II shows evidence of a forming dynamic stall vortex in the 20.15^o_u frames, though not as large as the DSV seen in the 20.15^o_u frames of Case I (Figures 4 and 5). This is, in large part, due to the later formation of the DSV in Case II, but also because the DSV in Case II is not as strong, as evidenced by vorticity values of smaller magnitude. The other major features of the pitching airfoil cycle, as discussed

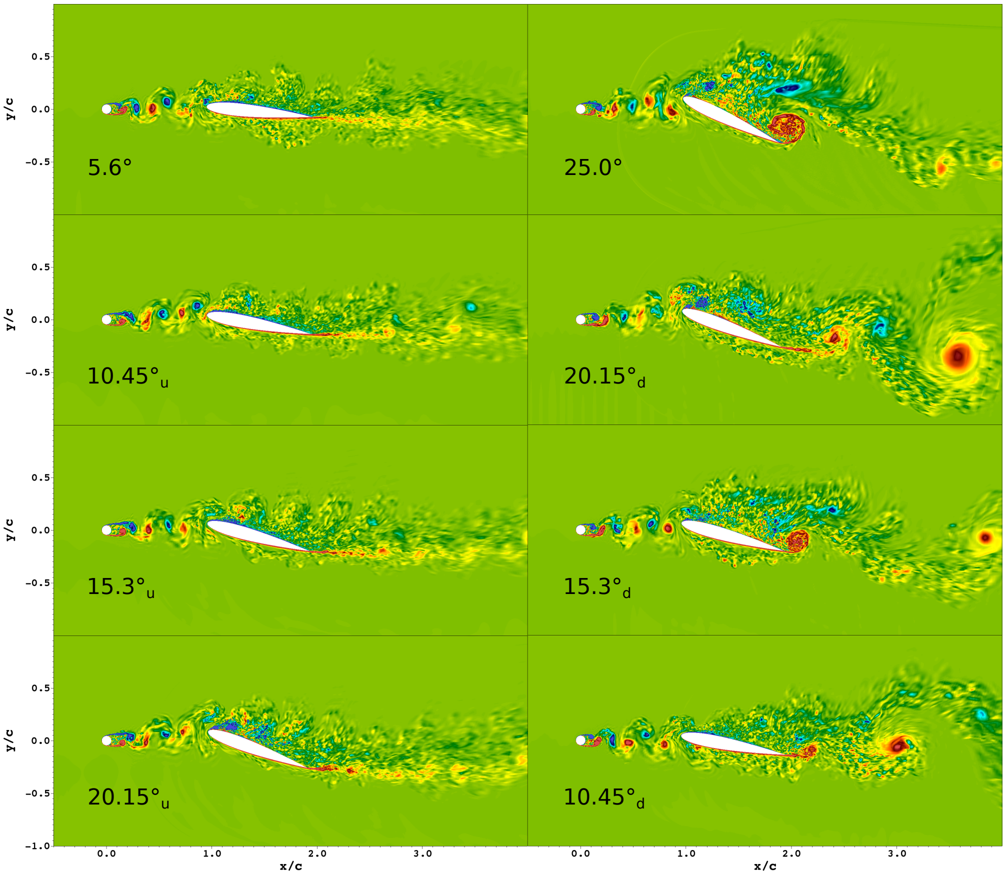

Figure 12. Zoomed-in spanwise averaged spanwise vorticity plots during the second cycle, at angles of attack posted in bottom left corner of each plot. The subscript 'u' denotes upstroke and 'd' downstroke. Darkest blue represents spanwise vorticity of less than $\omega_z U_\infty / c = -40$ (corresponding with clockwise fluid motion), and darkest red greater than $\omega_z U_\infty / c = 40$ (corresponding with counter-clockwise fluid motion).

in Section III.A, are also seen in the figures presented here, though with vortices formed at a later time. A comparison of the pressure coefficients along the suction side of the airfoils in Case I and II (Figure 13), again gives evidence of later vortex formation in Case II. The $\alpha = 20.15^o_u$ pressure profile plot shows that the DSV in Case I is roughly at the half chord distance (where the center of the vortex is determined by the lowest pressure values), while the DSV is forming at the leading edge of the airfoil in Case II. When the pitching airfoil begins its downstroke a second major vortex is formed at the leading edge. The $\alpha = 20.15^o_d$ plots shows evidence of the TEV in Case I resulting from the detachment of the second major vortex, while the pressure values in Case II show that the second major vortex is fairly weak and its center is located at about the half chord location.

	Case I	Case II
Vortex Center $(\frac{x}{c}, \frac{y}{c})$	(1.95,0.127)	(1.95,0.206)
Time (t^*)	27.9	29.3
Angle of Attack (α)	23.83^o_u	24.98^o_u
Vortex Strength (Γ)	10.547	7.453

Table 5. Properties of the DSV during the second pitching cycle of Cases I and II as the center of the vortex reaches the $x/c = 1.95$ position in the flow field.

The strength of the DSV in Case II is calculated as the center of the vortex crosses the $x/c = 1.95$ position in the flow field (Figure 14). A comparison with Case I (see Table 5) shows that the DSV in Case II crosses the $x/c = 1.95$ position with a much higher vertical position that the DSV in Case I ($y/c = 0.206$ in Case II versus $y/c = 0.127$ in Case I), and at a much later time ($t^* = 24.98$ in Case II versus $t^* = 23.83$ in Case I). The strength of the DSV in Case II is nearly %30 weaker than the DSV in Case I. In addition to

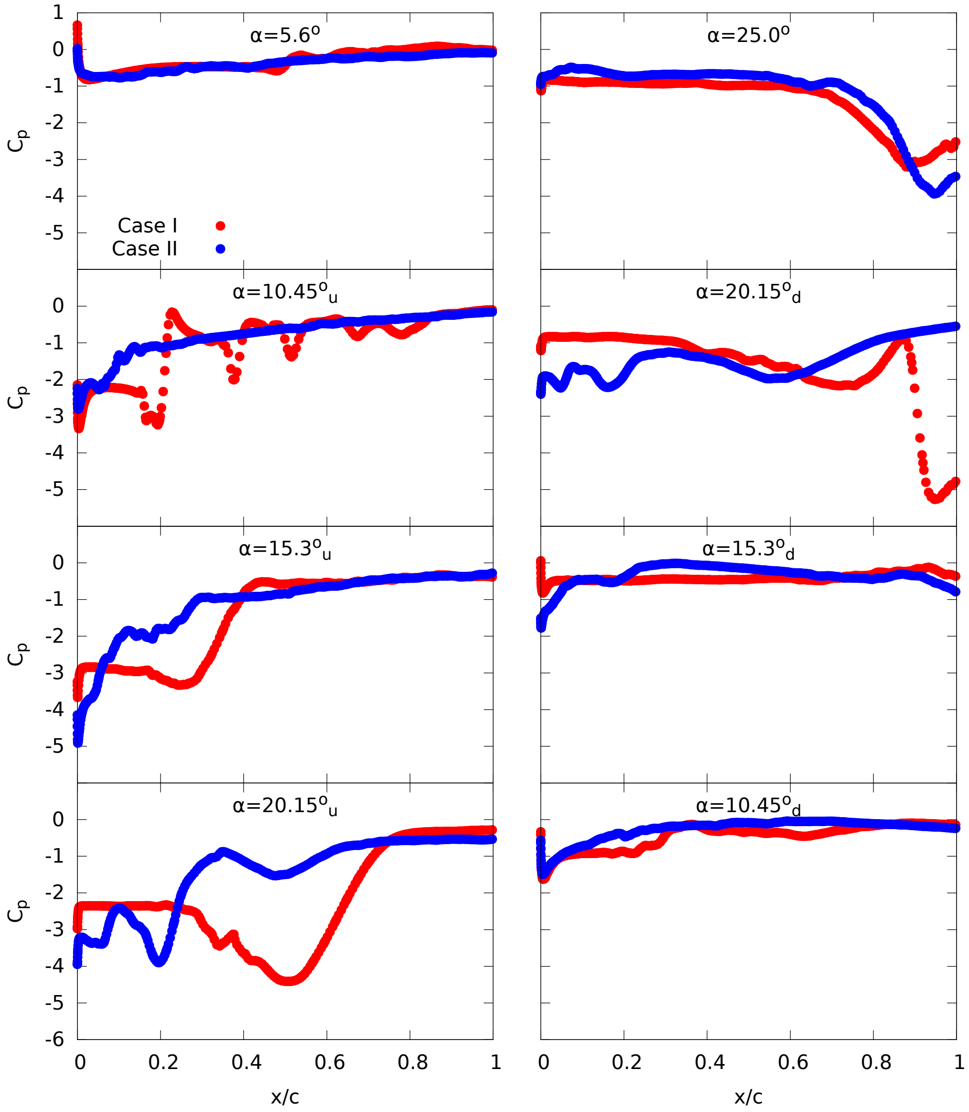

Figure 13. Spanwise averaged pressure coefficients along the suction surface of the airfoil for Cases I and II during the second cycle at angles of attack posted in the top center of each plot. The subscript 'u' denotes upstroke and 'd' downstroke.

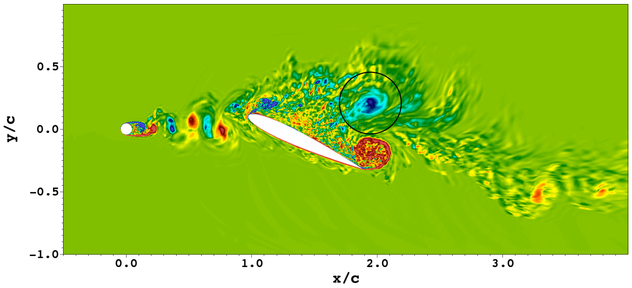

Figure 14. Spanwise averaged spanwise vorticity plot when the center of the DSV in the second cycle reaches $x/c = 1.95$ ($t^* = 29.3,\ \alpha = 24.99^o_u$) for Case II. The circle outlines the volume over which the integral of vorticity is taken.

the previous discussion of the later formation of the DSV in Case II, we also see that the vortices are not as strong when formed in the presence of incoming turbulence.

IV. Conclusion

A turbulent wake incident upon a pitching airfoil largely affects the forces and moments acting on the airfoil, and the flow structure of the fluid, including vortex formation. Dynamic stall of a pitching airfoil occurs at a later time (and larger angle of attack) when in the presence of a turbulent wake, due to the delayed formation, and thus detachment, of the dynamic stall vortex. While the maximum lift acting on the airfoil does not reach as large of values with upstream disturbances, the drag and magnitude of pitching moments are greatly reduced for most of the pitching cycle. In engineering applications, this reduced drag can lead to more efficient aerodynamic systems involving pitching airfoils, such as in rotary-wing flight and wind turbine power production. In addition, lower pitching moments decrease the structural strain on dynamically pitching blades and wings, potentially improving the life span of many mechanical systems. Weaker dynamic stall vortices shed from the airfoil in disturbed upstream flow leads to less intrusive vortex interactions with downstream structures, as in the case of blade-vortex interaction.

Future simulations will be performed to complete a third cycle for each of the cases presented here, where results will be analyzed and compared with the second cycle to determine whether approximations achieved during the second cycle accurately represent what should be expected in future cycles. Furthermore, a test case will be performed with the upstream cylinder at a lower vertical position with respect to the airfoil, and analyses will be performed to determine the effect of greater turbulence intensity on the pressure side of the airfoil in comparison with the two cases discussed here. A power spectral density (PSD) analysis will additionally be performed on the aerodynamic coefficients in these cases to determine how the turbulent wake affects the frequencies most important in determining the forces and moments on the airfoil. Similar tests will be performed to determine the effect of upstream disturbances on pitching airfoils with different Reynolds numbers, reduced frequencies, airfoil shapes, and turbulent inflow properties.

Acknowledgments

We would like to acknowledge support for this work given by the National Science Foundation grant CMMI-1250124 and thank the NSF XSEDE program for providing the computational resource allocation on the SDSC Comet cluster where the simulations were performed.

References

[1] Ham, N. and Garelick, M., "Dynamic stall considerations in helicopter rotors," *Journal of the American Helicopter Society*, Vol. 13, No. 2, 1968, pp. 49–55.

[2] Pierce, G., Kunz, D., and Malone, J., "The effect of varying freestream velocity on airfoil dynamic stall characteristics," *Journal of the American Helicopter Society*, Vol. 23, No. 2, 1978, pp. 27–33.

[3] Larsen, J., Nielsen, S., and Krenk, S., "Dynamic stall model for wind turbine airfoils," *Journal of Fluids and Structures*, Vol. 23, No. 7, 2007, pp. 959–982.

[4] Brady, W. and Ludwig, G., "Unsteady stall of axial flow compressors," Tech. rep., DTIC Document, 1963.

[5] Shi, Z.-W. and Ming, X., "Effects of unsteady freestream on aerodynamic characteristics of a pitching delta wing," *Journal of Aircraft*, Vol. 45, No. 6, 2008, pp. 2182–2185.

[6] Shi, Z. and Ming, X., "Experimental investigation on a pitching motion delta wing in unsteady free stream," *Modern Physics Letters B*, Vol. 23, No. 03, 2009, pp. 409–412.

[7] Carr, L., McAlister, K., and McCroskey, W., "Analysis of the development of dynamic stall based on oscillating airfoil experiments," Tech. rep., NASA Technical Note D-8382, 1977.

[8] McCroskey, W., "The phenomenon of dynamic stall." Tech. rep., DTIC Document, 1981.

[9] Ericsson, L. and Reding, J., "Fluid mechanics of dynamic stall part I. Unsteady flow concepts," *Journal of fluids and structures*, Vol. 2, No. 1, 1988, pp. 1–33.

[10] Choudhuri, P. and Knight, D., "Effects of compressibility, pitch rate, and Reynolds number on unsteady incipient leading-edge boundary layer separation over a pitching airfoil," *Journal of Fluid Mechanics*, Vol. 308, 1996, pp. 195–217.

[11] Visbal, M., "Numerical investigation of deep dynamic stall of a plunging airfoil," *AIAA journal*, Vol. 49, No. 10, 2011, pp. 2152–2170.

[12] Garmann, D. and Visbal, M., "Numerical investigation of transitional flow over a rapidly pitching plate," *Physics of Fluids (1994-present)*, Vol. 23, No. 9, 2011, pp. 094106.

[13] Gharali, K. and Johnson, D., "Effects of nonuniform incident velocity on a dynamic wind turbine airfoil," *Wind Energy*, 2014.

[14] Carr, L., "Dynamic stall progress in analysis and prediction," *Proceedings AIAA 12th Atmospheric Mechanics Conference, Snowmass, CO*, , No. AIAA paper 1985-1769, 1985.

[15] Kottapalli, S. and Pierce, G., "Drag on an oscillating airfoil in a fluctuating free stream," *Journal of Fluids Engineering*, Vol. 101, No. 3, 1979, pp. 391–399.

[16] Conger, R. and Ramaprian, B., "Pressure measurements on a pitching airfoil in a water channel," *AIAA journal*, Vol. 32, No. 1, 1994, pp. 108–115.

[17] Laneville, A. and Vittecoq, P., "Effect of turbulence on dynamic stall," *Wind Turbine Aerodynamics Seminar*, Sandia National Labs, 1985.

[18] Chen, J. and Choa, C.-C., "Freestream disturbance effects on an airfoil pitching at constant rate," *Journal of aircraft*, Vol. 36, No. 3, 1999, pp. 507–514.

[19] Gharali, K. and Johnson, D., "Dynamic stall simulation of a pitching airfoil under unsteady freestream velocity," *Journal of Fluids and Structures*, Vol. 42, 2013, pp. 228–244.

[20] Fischer, P., Lottes, J., and Kerkemeier, S., "nek5000 Web page," 2008, http://nek5000.mcs.anl.gov.

[21] Merrill, B. and Peet, Y., "High-order moving overlapping grid methodology for aerospace applications," *53rd AIAA Aerospace Sciences Meeting*, , No. AIAA paper 2015-1743, 2015.

[22] Panda, J. and Zaman, K., "Experimental investigation of the flow field of an oscillating airfoil and estimation of lift from wake surveys," *Journal of Fluid Mechanics*, Vol. 265, 1994, pp. 65–95.

[23] Schwarz, H., "Ueber einige abbildungsaufgaben." *Journal für die reine und angewandte Mathematik*, Vol. 70, 1869, pp. 105–120.

[24] Peet, Y. and Fischer, P., "Heat transfer LES simulations in application to wire-wrapped fuel," *Proceedings 10th AIAA/ASME Joint Thermophysics and Heat Transfer Conference*, 2010.

[25] Peet, Y. and Fischer, P., "Stability analysis of interface temporal discretization in grid overlapping methods," *SIAM Journal on Numerical Analysis*, Vol. 50, No. 6, 2012, pp. 3375–3401.

[26] Deville, M., Fischer, P., and Mund, E., *High-Order Methods for Incompressible Fluid Flow*, Vol. 9, Cambridge University Press, 2002.

[27] Donea, J., Huerta, A., Ponthot, J.-P., and Rodríguez-Ferran, A., "Arbitrary Lagrangian–Eulerian methods," *Encyclopedia of computational mechanics*, 2004.

[28] Bisplinghoff, R., Ashley, H., and Halfman, R., *Aeroelasticity*, Courier Corporation, 2013.